Richter, T., Sens-Schönfelder, C., Kind, R., Asch, G. (2014): Comprehensive observation and modeling of earthquake and temperature-related seismic velocity changes in northern Chile with passive image interferometry. - *Journal of Geophysical Research*, *119*, 6, p. 4747-4765.

DOI: http://doi.org/10.1002/2013JB010695

AGU PUBLICATIONS

JGR

Journal of Geophysical Research: Solid Earth

RESEARCH ARTICLE

10.1002/2013JB010695

Key Points:
- Superior sensitivity of velocity to stress and acceleration at Salar Grande
- Linear correlation between velocity decrease and PGA at single station
- Observation and modeling of velocity changes caused by thermal stresses

Supporting Information:
- Readme
- Figure S1
- Figure S2

Correspondence to:
T. Richter,
richter@gfz-potsdam.de

Citation:
Richter, T., C. Sens-Schönfelder, R. Kind, and G. Asch (2014), Comprehensive observation and modeling of earthquake and temperature related seismic velocity changes in northern Chile with passive image interferometry, *J. Geophys. Res. Solid Earth*, *119*, 4747–4765, doi:10.1002/2013JB010695.

Received 2 OCT 2013
Accepted 4 MAY 2014
Accepted article online 13 MAY 2014
Published online 2 JUN 2014

Comprehensive observation and modeling of earthquake and temperature-related seismic velocity changes in northern Chile with passive image interferometry

Tom Richter[1,2], Christoph Sens-Schönfelder[2], Rainer Kind[1,2], and Günter Asch[1,2]

[1]FR Geophysik, Malteserstraße, Freie Universität Berlin, Berlin, Germany, [2]Deutsches GeoForschungsZentrum GFZ, Telegrafenberg, Potsdam, Germany

Abstract We report on earthquake and temperature-related velocity changes in high-frequency autocorrelations of ambient noise data from seismic stations of the Integrated Plate Boundary Observatory Chile project in northern Chile. Daily autocorrelation functions are analyzed over a period of 5 years with passive image interferometry. A short-term velocity drop recovering after several days to weeks is observed for the M_w 7.7 Tocopilla earthquake at most stations. At the two stations PB05 and PATCX, we observe a long-term velocity decrease recovering over the course of around 2 years. While station PB05 is located in the rupture area of the Tocopilla earthquake, this is not the case for station PATCX. Station PATCX is situated in an area influenced by salt sediment in the vicinity of Salar Grande and presents a superior sensitivity to ground acceleration and periodic surface-induced changes. Due to this high sensitivity, we observe a velocity response of several regional earthquakes at PATCX, and we can show for the first time a linear relationship between the amplitude of velocity drops and peak ground acceleration for data from a single station. This relationship does not hold true when comparing different stations due to the different sensitivity of the station environments. Furthermore, we observe periodic annual velocity changes at PATCX. Analyzing data at a temporal resolution below 1 day, we are able to identify changes with a period of 24 h, too. The characteristics of the seismic velocity with annual and daily periods indicate an atmospheric origin of the velocity changes that we confirm with a model based on thermally induced stress. This comprehensive model explains the lag time dependence of the temperature-related seismic velocity changes involving the distribution of temperature fluctuations, the relationship between temperature, stress and velocity change, plus autocorrelation sensitivity kernels.

1. Introduction

Traditionally, seismic noise has been seen as useless and as a nuisance in the interpretation of seismic signals. However, seismic noise opens the field to a range of new applications by using noise-based Green's functions [*Shapiro and Campillo*, 2004] with other techniques as surface wave tomography or coda wave interferometry [*Snieder et al.*, 2002]. Especially monitoring applications benefit from the permanent availability of ambient noise, because the necessity of repeating sources, like earthquake multiplets or repeatable active sources, is eliminated.

Passive image interferometry introduced by *Sens-Schönfelder and Wegler* [2006] combines noise-based Green's functions with coda wave interferometry. The method is suitable for monitoring seismic velocities in the subsurface. *Sens-Schönfelder and Wegler* [2006] detected seasonal velocity changes caused by changes in fluid saturation of the medium due to precipitation and groundwater level changes. Seasonal velocity changes were also detected by *Meier et al.* [2010], *Hobiger et al.* [2012], and other authors. Coseismic velocity drops were detected for different events, e.g., the 2004 M_w 6.6 Mid-Niigata earthquake [*Wegler and Sens-Schönfelder*, 2007; *Wegler et al.*, 2009], the 2008 M_w 6.9 Iwate-Miiyagi Nairiku earthquake [*Hobiger et al.*, 2012], and the 2011 M_w 9.0 Tohoku earthquake [*Takagi and Okada*, 2012; *Sawazaki and Snieder*, 2013]. In most cases the velocity recovers in the course of several years after the earthquake. *Rivet et al.* [2011] related the velocity change due to a M 7.5 slow-slip event in Mexico not emitting any seismic waves to the strain rate. *Maeda et al.* [2010] speculated about a fluid-induced origin of velocity decreases correlating with earthquake swarms in a geothermal environment. *Sens-Schönfelder and Wegler* [2011] discussed possible reasons for coseismic velocity changes in a review of passive image interferometry.

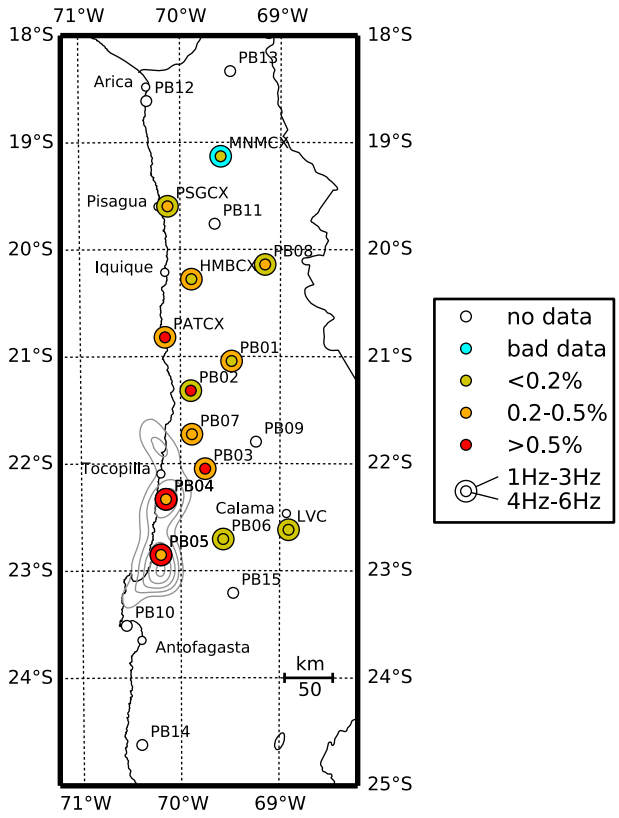

Figure 1. Map of the IPOC network indicating velocity decrease at the time of the Tocopilla earthquake at different stations in two different frequency bands. The rupture slip distribution from *Schurr et al.* [2012] is displayed in gray isolines (0.5 m to 3 m). Stations with no data had not yet been installed at the time of the Tocopilla event.

Here we report on earthquake-related drops of the seismic velocity at the time of the M_w 7.7 Tocopilla event (14 November 2007), and we specifically investigate station PATCX that additionally shows velocity drops after several smaller earthquakes and periodic variations that we model as caused by thermal stresses.

2. Data and Method

We use data from the Integrated Plate Boundary Observatory Chile (IPOC, http://www.ipoc-network.org/) operating in northern Chile since 2006 (Figure 1). The seismological part consists of 20 broadband stations with real-time data transmission. Additionally, data of station LVC from GEOFON (http://geofon.gfz-potsdam.de/) are used. The first station was installed in 2006, and at the time of the Tocopilla earthquake, 13 stations (including LVC) were running.

Cross correlations of different station pairs in the frequency band 0.01 Hz to 0.5 Hz do not show any distinct velocity change. Because we suppose a possible impact of the Tocopilla event on seismic velocity to be located near the surface, we use higher frequencies in this study. Above 1 Hz waves are subject to strong attenuation, and the coherence between cross correlations of station pairs is often lost depending on the interstation distance. Autocorrelations, of course, do not have this shortcoming and are therefore analyzed in this study.

Before calculating the autocorrelation, the data have to be prepared. We use the vertical component of the data. For each day, we detrend, filter, and downsample the data to 50 Hz. Finally, the data have to be normalized to reduce the effects of earthquakes in the correlations. An overview of normalization methods was presented by *Bensen et al.* [2007]. In northern Chile we have to deal with a high amount of local seismicity which leads to corrupt noise correlations for some days even when normalization is applied. This is because earthquakes do not only have a higher amplitude than noise which is successfully dealt with by the normalization but also occur during a significant time span. Therefore, we suppress a part of the earthquakes completely with an automated method. Samples with an envelope larger than 10 times the root-mean-square of the envelope in quiet periods are set to zero. We then additionally apply the 1 bit normalization. All samples are set to +1 if they are positive and −1 if they are negative. Gaps and data suppressed in the first step stay at zero. This combined normalization approach enhances the noise correlation of days with numerous local events. The quality of noise correlations of interesting days immediately after moderate earthquakes is improved in spite of a potentially large number of aftershocks.

Daily autocorrelations are computed in the frequency domain by calculating the square of the absolute value of the Fourier spectrum for all available data. The daily autocorrelations are normalized after back transformation to the time domain so that the value at 0 s lag time equals 1. These autocorrelations are used as input for the passive image interferometry.

Relative traveltime variations can be determined for different lag time windows in the autocorrelation functions that start at t_1 and end at t_2. We use the 5 s long time windows (5 s, 10 s), (10 s, 15 s), and (15 s, 20 s).

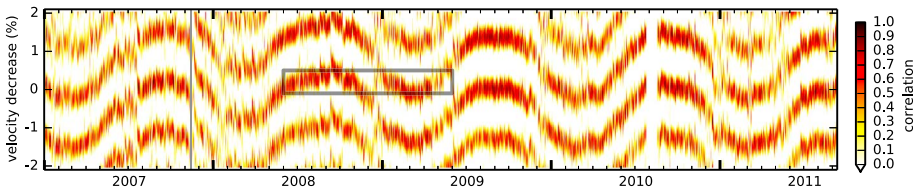

Figure 2. Similarity matrix of the autocorrelation function at PATCX for the frequency band 9 Hz to 11 Hz and lag time window 7 s to 9 s as produced by equation (1) for different days. The vertical line marks the time of the Tocopilla earthquake. The relative velocity changes cause neighboring phases to occur at the same lag time for different times in the year (see box). This corresponds to a phase shift of 2π between the respective noise correlation functions. We adapted the interferometry method to deal with this—first by the iterative reference calculation described in section 2, second by the alternative fitting procedure for long-term changes in section 3.2.

First, a reference autocorrelation ϕ_{ref} is computed as the mean over all available daily autocorrelations for this station. Then the daily autocorrelations ϕ_{d} are stretched and compressed on the time axis with respect to zero lag time. For determining traveltime fluctuations, the similarity between the unstretched reference and the stretched daily autocorrelation function in the chosen time window is determined for each stretching factor ϵ by the correlation coefficient

$$\text{cc}(\epsilon) = \frac{\int_{t_1}^{t_2} \phi_{\text{d}}(t(1+\epsilon))\phi_{\text{ref}}(t)\text{d}t}{\left(\int_{t_1}^{t_2} \phi_{\text{d}}^2(t(1+\epsilon))\text{d}t \int_{t_1}^{t_2} \phi_{\text{ref}}^2(t)\text{d}t\right)^{1/2}} \tag{1}$$

adopting values between +1 and −1. The stretching factor with the highest similarity can be directly translated into relative traveltime variation $-\Delta t/t$, which corresponds to the relative velocity change $\Delta v/v$ if this change is homogeneous:

$$\epsilon = -\frac{\Delta t}{t} = \frac{\Delta v}{v}\,. \tag{2}$$

For an illustration of this method we refer to *Wegler et al.* [2009, Figure 3]. This procedure can be repeated for every available daily autocorrelation to construct a similarity matrix which displays the correlation coefficients $\text{cc}(\epsilon)$ for the different stretching factors ϵ for each day. The maxima of the similarity matrix for each column (day) can be used to trace the relative velocity change over time. Both observed velocity changes and stretching factors will be termed ϵ in the following. If the velocity change is not homogeneous in space, we obtain an apparent relative velocity change that we also term ϵ.

As we work in a comparably high frequency range, we observe the velocity variations to cause phase shifts at late lag times that are significant compared to the dominant period. Consequently, a reference correlation function ϕ_{ref} calculated by simple stacking of all daily autocorrelation functions will be deteriorated, because correlation functions from different periods interfere destructively for high frequencies (Figure 2). We therefore introduce a new scheme to calculate the reference autocorrelation in an iterative manner. Using a stack of the correlation functions as preliminary reference, we first obtain a preliminary estimate ϵ_{prel} of the relative velocity variations. The final reference function is not calculated as the mean of daily autocorrelations over all N days t_i, as before, but as the mean of all autocorrelations corrected for the preliminary estimate of the velocity change ϵ_{prel}:

$$\phi_{\text{ref}}(t') = \frac{1}{N}\sum_{i=1}^{N} \phi_{\text{d}}(t'(1-\epsilon_{\text{prel}}(t_i)))\,. \tag{3}$$

This enhances the resulting correlation between the reference and the stretched daily correlation functions and thus improves the measurements when dealing with high frequencies or late lag times as in Figure 2. We will come back to the iterative reference calculation in sections 3.2 and 3.5.

Zhan et al. [2013] demonstrated that spurious velocity changes can be caused by changes in the ambient noise frequency content. A stretching of the amplitude spectrum can introduce spurious velocity changes if measured with the stretching technique at early lapse times. Scaling the tests performed at a frequency of 0.1 Hz by *Zhan et al.* [2013] to the frequency and lapse times used in the present study, we can be sure that this effect would be smaller than 2×10^{-2}% even for the rather extreme case of a perfect frequency stretch

of 20%. Moreover, in contrast to the test by *Zhan et al.* [2013] the time windows used here contain multiple wave packets. In this case also an ideal velocity change in the medium introduces a stretch in the amplitude spectrum of the Green's function, independently of the source spectrum. Consequently, a change in the amplitude spectrum does not indicate that an observed velocity change is spuriously caused by a change in the source spectrum.

3. Observations

3.1. Velocity Changes Associated With Tocopilla Event

Autocorrelations of all stations installed at the time of the Tocopilla earthquake are analyzed using the method described in the previous section. We use the two frequency bands 1–3 Hz and 4–6 Hz for the analysis. An electronic supplement shows the daily autocorrelation functions for all analyzed stations and the respective results of the stretching procedure, i.e, the similarity matrices. A velocity drop larger than 0.2% is detected at the time of the Tocopilla earthquake at 10 of 13 running stations (Figure 1). Stations PB04 and PB05 located near the maxima of the slip distribution as calculated by *Schurr et al.* [2012] show the highest velocity drop in the 1–3 Hz frequency band (Appendix A). Station PATCX more than 100 km north of the epicenter and outside the rupture area shows the highest velocity drop in the 4–6 Hz frequency band. At all stations except for stations PB05 (1–3 Hz) and PATCX (4–6 Hz) the velocities return to the level before the earthquake in several days to weeks. In the case of stations PB05 and PATCX this recovery takes about 2 years (Figure 3a, Appendix A).

3.2. Long-Term Velocity Changes at Station PATCX

Contrary to the other IPOC stations, station PATCX shows additional velocity drops at smaller earthquakes and periodic annual velocity changes. Figure 3a presents the results from the stretching procedure for station PATCX in the 4 Hz to 6 Hz frequency band for lag times from 10 s to 15 s together with daily mean temperatures at Iquique airport. First-order observations are the annual velocity change which correlates to temperature and a velocity drop at the time of the Tocopilla earthquake recovering in the course of around 2 years. We can fit these observations with the function

$$\begin{aligned}\epsilon_{\mathrm{mod}}(t) = \epsilon_0 + \epsilon_{\mathrm{P}} \cos\left[\frac{2\pi}{1\mathrm{yr}}(t - t_{\mathrm{P0}} - t_P)\right] \\ - \epsilon_{\mathrm{EQ}} \exp\left(-\ln 10 \frac{t - t_{\mathrm{EQ0}}}{t_{\mathrm{EQ}}}\right) H(t - t_{\mathrm{EQ0}})\end{aligned} \tag{4}$$

with t_{P0} marking the day 1 January 2010 and t_{EQ0} marking 14 November 2007, the day of the Tocopilla earthquake. H is the Heaviside function yielding 0 for negative arguments and 1 otherwise. The fitting parameters are associated with different causative processes. ϵ_P is the amplitude of the relative velocity change with annual period. t_P is the phase of the maximum velocity of this periodic change relative to 1 January 2010. ϵ_{EQ} is the amplitude of the velocity drop at 14 November 2007 and t_{EQ} the recovery time to 10% of this earthquake-related change. The meaning of these four parameters is indicated with thick, black arrows in Figure 3a. ϵ_0 is a constant offset and of no further importance.

For calculating the five optimal fitting parameters the most obvious solution would be to minimize the sum of the quadratic difference between ϵ_{mod} and the stretching factor with the best similarity over all N days t_i: $\sum_{i=1}^{N}(\epsilon_{\mathrm{mod}}(t_i) - \epsilon_{\mathrm{max}}(t_i))^2$. This strategy, however, has two serious drawbacks: First, days with erroneous outliers tend to be overweighted. Second, due to cycle skip the maxima of the similarity matrix could be at neighboring phases for different days as illustrated by Figure 2. To avoid such cycle skipping, we maximize the mean of correlation coefficients at the stretching factors ϵ_{mod}

$$\mathrm{cc}_{\mathrm{mean}} = \frac{1}{N}\sum_{i=1}^{N} \mathrm{cc}(\epsilon_{\mathrm{mod}}(t_i)) \,. \tag{5}$$

This approach finds the model curve which runs along the highest ridge of the similarity matrix. The optimization uses the Nelder-Mead simplex algorithm [*Nelder and Mead*, 1965; *Wright*, 1996] implemented in the SciPy library [*Jones et al.*, 2001] with reasonable starting values. We use the estimated long-term velocity changes ϵ_{mod} for the a posteriori calculation of the reference trace introduced in section 2 ($\epsilon_{\mathrm{prel}} = \epsilon_{\mathrm{mod}}$)

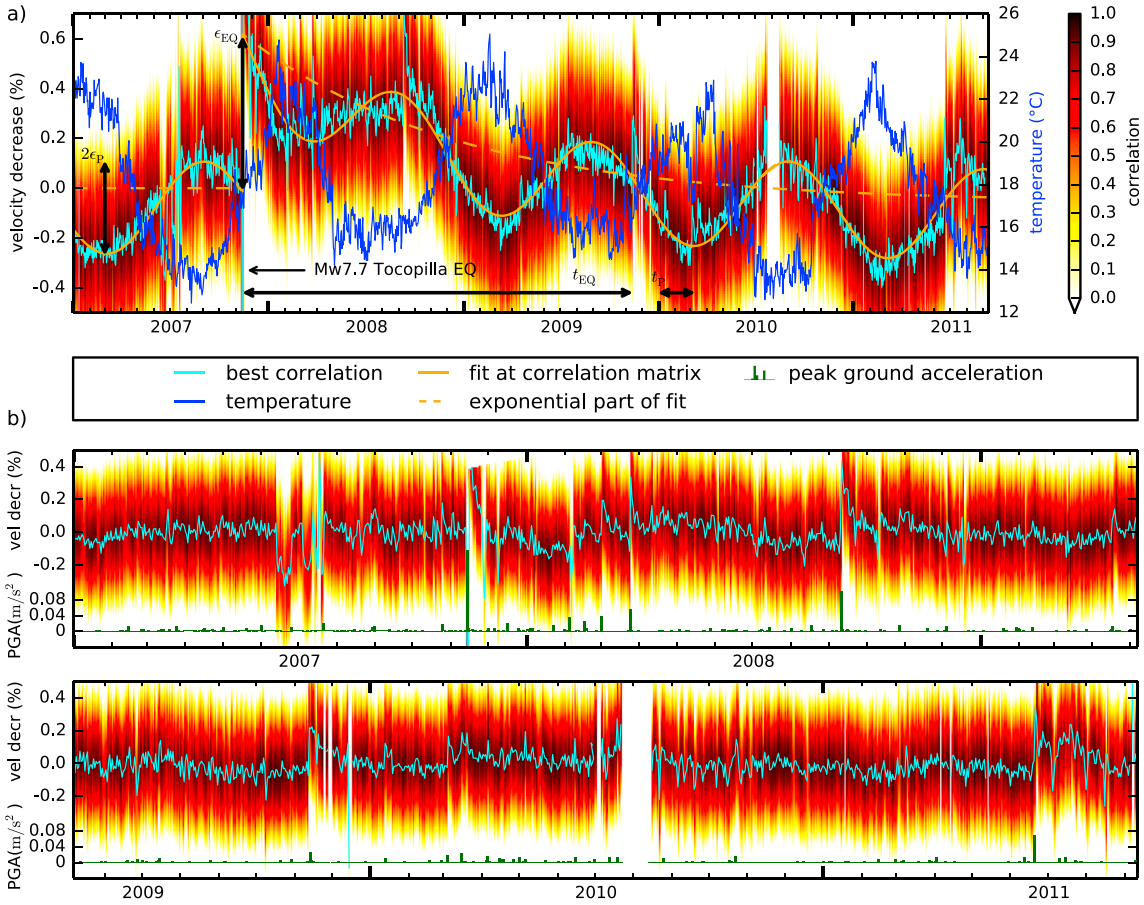

Figure 3. (a) Similarity matrix of station PATCX for the time window of 10 s to 15 s of the autocorrelation function in the frequency band 4 Hz to 6 Hz. The stretching factors resulting in the best correlation to the reference trace for each day are connected by a cyan line and represent the observed velocity variations. Note that the *y* axis displays velocity *decrease* ($-\epsilon$). There is a clear correlation between temperature variations (blue line, daily mean temperature at Iquique airport) and the periodic component of the velocity changes. Additionally, there is a sudden drop of seismic velocity at the time of the Tocopilla earthquake. Seismic velocity is recovering to the level before the Tocopilla event in the course of around 2 years. These two effects are fitted to the similarity matrix with an exponentially decaying offset (broken orange line) added to a sinusoidal function (orange line). The fitting parameters amplitude of periodic relative velocity change ϵ_P, amplitude of coseismic relative velocity drop ϵ_{EQ}, phase of periodic velocity change t_p, and recovery time of coseismic velocity drop t_{EQ} are marked by thick, black arrows. (b) Same similarity matrix as described in Figure 3a with long-term effects subtracted. Therefore, the orange line in Figure 3a was used. Additionally, the peak ground acceleration for each day is plotted at the bottom. A clear correlation between peak ground acceleration and short-term velocity drops can be observed. Most of the high values of peak ground acceleration (PGA) originate from local earthquakes within 200 km with a magnitude above 5.5. An apparent velocity increase is visible in June and July 2007. We ignore this change as it is related to a low correlation and probably unphysical.

and repeat the calculation of the similarity matrix and the fitting. For the plot in Figure 3a the final optimal parameters are

$$\epsilon_P = 0.19\%, \qquad \epsilon_{EQ} = 0.68\%, \qquad \epsilon_0 = -0.10\%,$$
$$t_P = 61\text{d} \qquad \text{and} \qquad t_{EQ} = 770\text{d}\,.$$

3.3. Shaking-Induced Velocity Changes at PATCX

Here we analyze short-term velocity changes not contained in the above model. Removing the long-term trend at station PATCX as provided by the function in equation (4) produces the plot in Figure 3b. An additional short-term velocity decrease at the time of the Tocopilla earthquake shows an overlap of different effects with different timescales. At other days velocity drops can be observed, too, recovering in the course of several days to 1 month. Such days show a high peak ground acceleration caused by regional earthquakes as indicated by the green bars at the bottom of Figure 3b. The bar plot shows the peak ground acceleration on the vertical component of each day as it was sensed by an accelerometer right next to the seismometer. We measure the amplitude of the short-term velocity decreases by taking the difference of mean velocity during the 10 days prior to the event and minimum velocity after the event with a correlation above 0.5

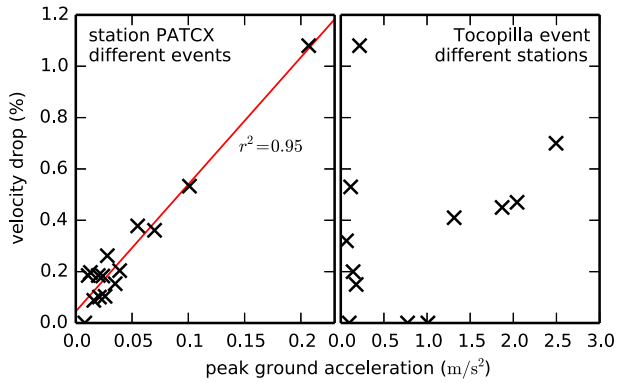

Figure 4. Seismic velocity decrease as a function of peak ground acceleration (left) for different events at station PATCX and (right) for the Tocopilla event at different stations. A linear relationship of seismic velocity drop and peak ground acceleration can be observed at station PATCX. This relationship does not hold true when considering different stations because of different environmental settings.

times the preevent correlation value. Figure 4 (left) reveals a linear relationship between the peak ground acceleration of events exceeding an acceleration of 0.01 m/s^2 and the amplitude of corresponding velocity drops for station PATCX. Notice that the data point for the Tocopilla earthquake at station PATCX consists of the long-term velocity decrease ϵ_{EQ} and the additional short-term velocity decrease determined here. In contrast, a linear relationship does not exist when comparing the velocity decrease caused by the Tocopilla earthquake at different stations as presented in Figure 4 (right). Obviously, the media around different stations have different sensitivity to velocity changes caused by ground acceleration.

Hobiger et al. [2012] analyzed peak ground accelerations and coseismic velocity changes observed with cross correlations for the 2008 *M* 6.9 Iwate earthquake at different stations. They found a trend linking strong acceleration to high velocity drops. Considering the scatter and the averaging of station sensitivities inherent to their inversion procedure the relation is not very clear. Both *Takagi and Okada* [2012] and *Sawazaki and Snieder* [2013] found for the *M* 9.0 Tohoku earthquake that amplitudes of coseismic changes are in a better agreement with dynamic strain data than peak ground acceleration. Maxima of dynamic strain are estimated with the ratio of peak ground velocity and average shear velocity of the uppermost 30 m. We analyze for the first time coseismic velocity changes for different events at a single station which guarantees constant sensitivity. Dynamic strain is in this case proportional to the peak ground velocity. Our results favor a linear relationship to peak ground acceleration (coefficient of determination $r^2 = 0.95$ for the linear regression) over dynamic strain ($r^2 = 0.79$). We emphasize that this comparison is only possible at station PATCX because its superior sensitivity results in a velocity response to the moderate shaking caused by numerous small events, whereas other stations respond only to the largest events.

3.4. Velocity Changes in the Course of 1 Day

Section 3.2 suggests that the long-term periodic velocity changes at station PATCX are related to temperature variations. Still, other factors showing a similar annual periodicity as temperature could result in a similar effect. Precipitation or groundwater level changes are unlikely to cause the velocity changes because of the Atacama desert's very dry conditions. Hydrological effects might be observed due to lateral flow in the vicinity of the river valleys that transect the desert. But such effects are unlikely as regular as the observed velocity variations that are well fitted by a sine curve. Especially, the changes with a daily period are unlikely to be caused by groundwater flow. Here daily velocity changes are analyzed at station PATCX to test the hypothesis that velocity changes are temperature related.

For calculating the daily velocity changes, we autocorrelate the 4 Hz to 6 Hz data in bunches of 1 h with an overlap of half an hour. We then perform the stretching procedure for the 48 autocorrelations for each day using the mean of all functions of this day as a reference. The result is demeaned and days with less than 48 data points because of missing data are discarded. Finally, the stretching factors with the highest correlation coefficient and of the same hour of day are stacked for all remaining 1570 days. Figure 5 shows the velocity changes together with error bars of a length of twice the standard error of the mean. The mean of the correlation coefficients of each hour of the day are displayed in Figure 5 (right). We observe a daily relative velocity change with a peak-to-peak value of around 0.18% for 5 s to 10 s lag time and a peak-to-peak value of 0.04% for the later two time windows. For larger lag times the errors tend to be higher, and the correlation coefficient tends to be lower. The mean air temperature over all available days is plotted together with the daily velocity changes in Figure 5 (left). The temperature data come from a creepmeter installation (station CHO2) 32 km south of station PATCX with a similar distance to the coast and a similar elevation as PATCX. The velocity change measurements show the same pattern as the air temperature. The only difference is a

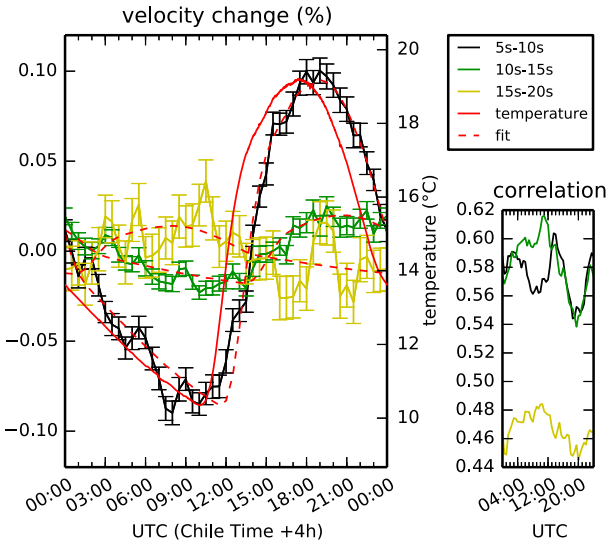

Figure 5. Velocity change at station PATCX in the course of 1 day for three different time windows of the autocorrelation function compared to air temperature (red line). Additionally a fit (stretched on y-axis and delayed on *x* axis) of the temperature curve to the observations is shown (dashed red lines). The velocity changes follow clearly the course of the temperature with a time delay of 1.5 h, 3.3 h and 14.5 h for the 5−10*s*, 10−15*s*, and 15−20*s* window, respectively. Data for the last time window have low correlation and high error bars as compared to the first two time windows, and fits the temperature least well.

phase shift of 1.5 h, 3.3 h, and 14.5 h between the two measurements for the lag time windows 5−10 s, 10−15 s, and 15−20 s, respectively. The almost perfect fit of the velocity change and the phase-shifted temperature curve is a strong indication that velocity changes are caused by changes of air temperature. It supports the idea that temperature changes are also responsible for the annual variations of subsurface velocities. We discuss amplitude and phase of the periodic velocity variations in section 4.

3.5. Frequency and Lapse Time Dependence of Long-Term Velocity Changes

Now we analyze long-term velocity changes at station PATCX as a function of frequency and lag time. Therefore, we filter the data in the preparation step (before autocorrelation and normalizations) with different frequency bands ranging from 2 Hz to 12 Hz. The rest of the processing is the same as described in section 2 except that lag time windows of 2 s length are chosen as input into the stretching procedure to increase the resolution in lapse time.

To easily compare the long-term velocity changes, we compare the parameters of the fit function ϵ_{mod}. Figure 6 (top) displays the amplitude of the annual periodic velocity change ϵ_{P}, the velocity drop due to the Tocopilla event ϵ_{EQ}, and the parameter that was maximized during the optimization process—the mean correlation at the different stretching factors ϵ_{mod}. Figure 6 (bottom) displays the phase delay between annual periodic velocity change and air temperature change $t_P - t_{\text{temp}}$ and the recovery time of the coseismic drop to 10% t_{EQ} is together with a legend and mean autocorrelations. All parameters are displayed as a function of lag time and frequency. The phase of the temperature $t_{\text{temp}} = 30$d is determined from a sensor at the creepmeter station CHO2 in around 50 cm depth. We can observe the following features:

1. The mean correlation generally decreases with higher lag time, because the fraction of waves contributing to the autocorrelation function is decreasing compared to random energy. This effect is even larger for high frequencies. The coherence is therefore completely lost for late lag times and high frequencies.
2. The amplitude of the periodic velocity change ϵ_P ranges from 0.1% for low frequencies to 0.8% for high frequencies. Trends we observe are higher amplitudes for higher frequencies and slightly lower amplitudes for later lag times.
3. The amplitude of the Tocopilla earthquake-related velocity change ϵ_{EQ} ranges from 0.5% to 1.2%. We observe the same trend—higher amplitudes for higher frequencies—as for ϵ_P. The magnitude of frequency dependency, however, is much smaller. It is just a factor of around 1.6 for amplitudes between 7−9 Hz and 2−4 Hz compared to a factor of 4 for ϵ_P. The amplitude is constant with lag time for most frequencies.
4. The phase delay between periodic velocity changes and the temperature $t_P - t_{\text{temp}}$ is around 30 days for late lag times and most frequencies. For earlier lag times the phase tends to be smaller for low frequencies (except 2 Hz to 4 Hz) and higher for high frequencies.
5. The recovery time t_{EQ} is nearly independent of lag time and frequency and is around 2 years.

Two major points that we want to highlight are first that we observe higher amplitudes for higher frequencies, both for ϵ_P and ϵ_{EQ}, and second that this effect is larger for ϵ_P than for ϵ_{EQ}. If we assume higher frequencies to be more sensitive to shallow depth (which is reasonable, e.g., for multiple-scattered bulk

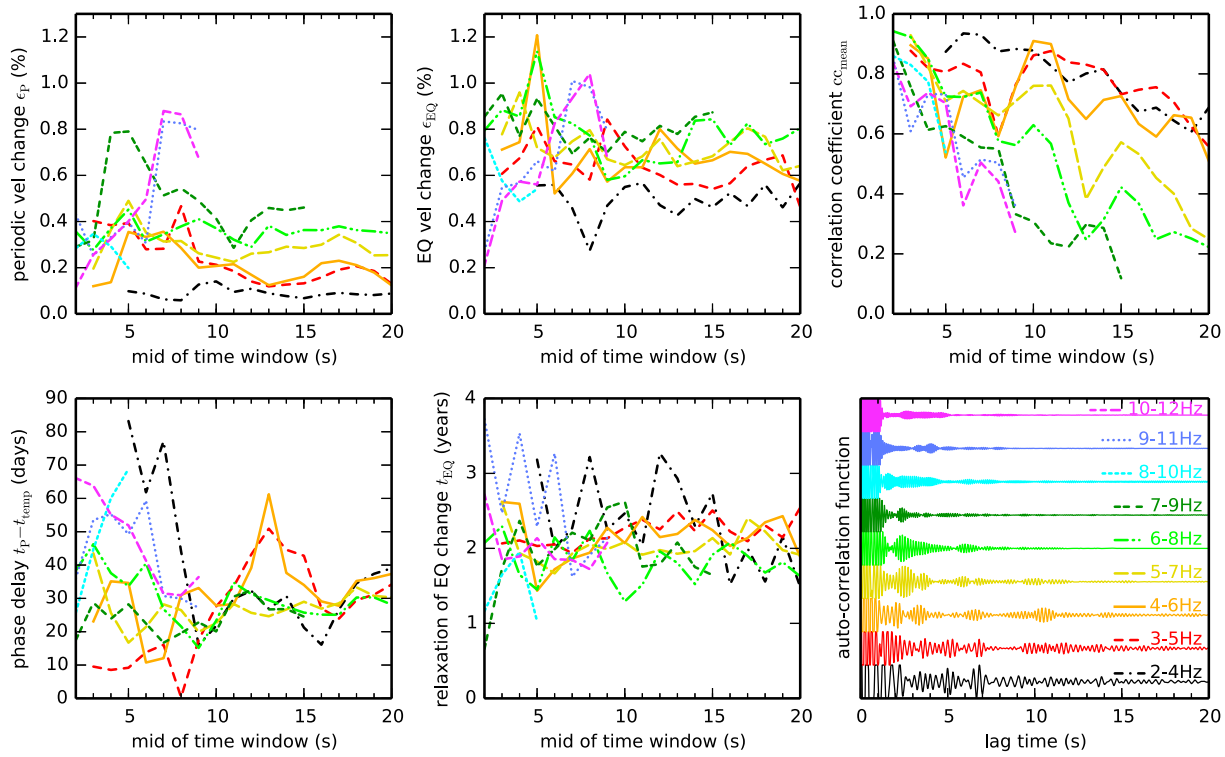

Figure 6. Fitting parameters of equation (4) corresponding to the thick arrows in Figure 3 and the optimized mean correlation coefficients cc_{mean} as a function of lag time window and frequency band for station PATCX. The width of the time windows is 2 s, and the data are filtered in the frequency band before performing the autocorrelation and normalization. Bottom left figure displays the phase delay of the periodic change against the phase of the temperature course. Bottom right figure shows the legend and the mean autocorrelation functions with values above 0.02 clipped.

waves due to the increased scattering of high-frequency waves), we can conclude qualitatively that the local velocity variation is stronger at shallow depth than at deeper depth and that the periodic local velocity change is located more shallow than the earthquake-induced velocity change. This fact adds another indication that the periodic velocity changes are induced by a shallow penetrating fluctuation of atmospheric temperature.

4. Model for Periodic Velocity Change

4.1. Temperature Fluctuations in the Subsurface

Our results for station PATCX show a velocity variation with annual and daily period. Section 3.3 indicates that these changes are caused by changes of the subsurface temperature. Furthermore, station PATCX shows, contrary to all other stations, velocity drops at low ground accelerations. The environment of station PATCX is strongly influenced by sedimented salt in the whole area including the nearby Salar Grande (Figure 7). This is not the case for the other IPOC stations, even for PB02 which is at a similar distance but upslope from the Salar Grande. We therefore suspect that the particular geological conditions at station PATCX are the reason for the medium's superior sensitivity to ground acceleration and temperature changes.

To improve our understanding of the periodic velocity changes, we model the effect of temperature changes with periods of 1 day and 1 year. Our aim is to demonstrate that temperature changes are able to explain the observed velocity changes with reasonable medium parameters. This is specifically motivated by the fact that studies of elastic constants and their temperature derivatives generally show a negative correlation between seismic velocity and temperature for constant pressure [e.g., *Anderson et al.*, 1968, Table 1], opposite to our observations, which show a positive correlation. A possible process explaining this discrepancy is thermally induced stressing. Increased temperature can lead to stress buildup. This again changes elastic properties and the velocity of the medium [*Toupin and Bernstein*, 1961, and references therein].

Here we construct a model based on thermal stressing which explains our observations. We have to consider the following: distribution of temperature fluctuation in the subsurface, thermally induced stress, its

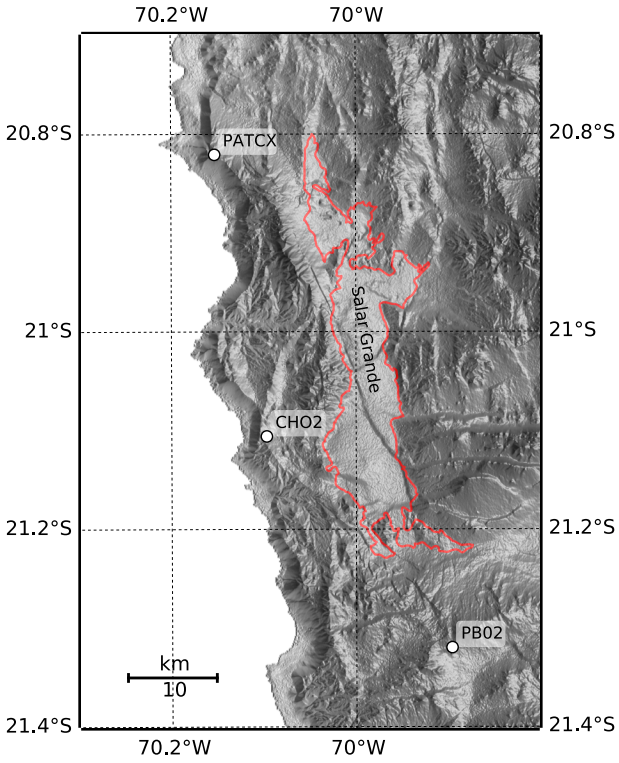

Figure 7. Shaded relief map with seismic stations PATCX, PB02, and creepmeter installation CHO2. Contour of Salar Grande is from *Reijs and McClay* [1998]. The environment of station PATCX is influenced by salt sediment, unlike PB02, which is at a similar distance but upslope from the Salar Grande.

implications on local velocity changes, and finally, autocorrelation sensitivity kernels to model the phase delay and amplitude of velocity changes observed in the autocorrelation function.

For modeling the subsurface temperature fluctuations T we assume a temperature fluctuation field at the surface of

$$T(x, z = 0, t) = T_0 \frac{1 + \cos kx}{2} e^{i\omega t} \quad (6)$$

as similarly described by *Berger* [1975]. T_0 is the amplitude, ω the angular frequency, and k the wave number of the spatial fluctuations. Cartesian coordinates x, y, and z point eastern, southern, and downward, respectively. The term $(1 + \cos kx)/2$ represents the influence of topography and the ocean [*Berger*, 1975]. Its wavelength $2\pi/k$ is in the order of several kilometers. Station PATCX is located around 3 km away from the ocean. We assume $k = 2\pi/10$ km so that for the station near $x = 0$ temperature fluctuations over the ocean are small with no fluctuations 2 km away from the coast. With the approximation $k^2 \ll \omega/\kappa$ valid for typical values of k, ω, and thermal diffusivity κ, we can ignore horizontal heat conduction. The solution of the heat conduction equation then reads

$$\begin{aligned} T(x, z, t) &= T_0 \frac{1 + \cos kx}{2} e^{i(\omega t - \gamma z) - \gamma z} \\ &= T(x, z = 0, t) e^{-(1+i)\gamma z} \text{ with } \gamma = \sqrt{\frac{\omega}{2\kappa}}. \end{aligned} \quad (7)$$

The resulting temperature fluctuations are exponentially decreasing with depth, and they are subject to a phase delay increasing with depth. At the skin depth $z = 1/\gamma$ the amplitude of the signal is $1/e$ compared to the amplitude at the surface and the phase delay is 1 rad.

We can determine κ and T_0 from daily and annual temperature fluctuations with the help of temperature sensors installed at the creepmeter station CHO2 32 km south of PATCX. *Bach* [2010] describes an experiment with four temperature sensors installed at different depth for a period of 4 days. The absolute values of the daily temperature fluctuation are taken from Table 3.1, and the phase shifts are estimated from Figure 3.5 of *Bach* [2010]. The data point for annual temperature fluctuation is taken from the temperature sensor installed directly at the creepmeter buried at around 50 cm depth. These data points and the expected temperature variation with depth for annual and daily periods are displayed in Figure 8.

By fitting the data points we infer values for the thermal diffusivity of $\kappa = 0.3$ mm^2/s, the peak-to-peak amplitude of daily temperature fluctuation $2T_{0d} = 38$ K, and amplitude of annual temperature fluctuation $2T_{0a} = 12$ K (assuming $x = 0$). The resulting skin depth is 1.9 m for annual and just 10 cm for daily changes (Table 1). The daily temperature fluctuations directly at the surface are larger than the daily air temperature variations of around 9 K because of heating by absorption of radiation.

4.2. Thermally Induced Stress

The next step is the calculation of stress changes induced by the fluctuating temperature. *Berger* [1975] thoroughly analyzed the relation between these two quantities with a "plane strain" assumption. *Ben-Zion and Leary* [1986] added unconsolidated cover at the surface to Berger's model. The unconsolidated layer takes

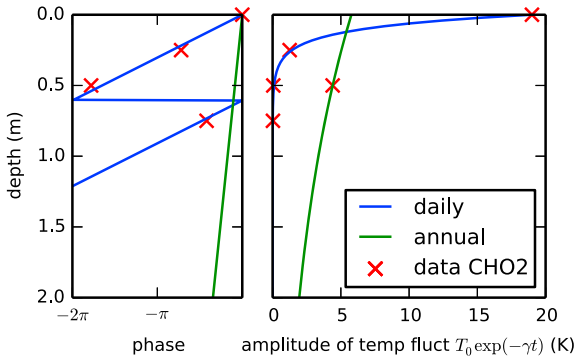

Figure 8. Phase and absolute value of daily and annual temperature fluctuations as a function of depth. The skin depth is 1.9 m for annual and just 10 cm for daily changes. The respective peak-to-peak amplitudes are 12 K and 38 K. Data points of daily temperature fluctuations are from *Bach* [2010].

part in the diffusion of heat but does not support stress. This leads to a larger time delay between surface temperature and strain which better fits their data. *Tsai* [2011] tried to explain periodic velocity variations observed by *Meier et al.* [2010] in Southern California with these models.

Berger [1975] describes thermally induced stress by supplying the stress-strain relationship with an additional term to allow for thermal expansion :

$$\varepsilon_{ij} = \frac{1+\nu}{E}\sigma_{ij} - \left(\frac{\nu}{E}\sum_k \sigma_{kk} - \alpha T\right)\delta_{ij}\,. \quad (8)$$

Here ε is strain, σ stress, E the Young's modulus, ν Poisson's ratio, α the linear expansion coefficient, T temperature variation, and δ_{ij} is the Kronecker delta which yields 1 for $i = j$ and 0 otherwise. The stress change is estimated as a linear superposition of the principal stresses in all three directions

$$\sigma = \sigma_{xx} + \sigma_{yy} + \sigma_{zz}\,. \quad (9)$$

Using equation (8) and the plane strain assumption $\varepsilon_{yy} = 0$, we express the stress as a function of strains and temperature fluctuation:

$$\sigma = \frac{E}{1-2\nu}(\varepsilon_{xx} + \varepsilon_{zz} - 3\alpha T)\,. \quad (10)$$

Finally, we insert the solution of *Berger* [1975, equation (8), reproduced in Appendix B] for the approximation $k \ll \gamma$ together with our temperature field from the previous section to get

$$\sigma = \frac{\alpha E T(z=0)}{1-\nu}\left(-2e^{-(1+i)\gamma z} + (1+\nu)(1-i)\frac{k}{\gamma}e^{-kz}\right) \quad (11)$$

neglecting one term with k^2/γ^2. We expect higher velocities for compressional stress, which corresponds to negative (extensional) stress σ. The compressional stresses $-\sigma_{xx}$, $-\sigma_{yy}$, $-\sigma_{zz}$, and $-\sigma$ are plotted in Figure 9 at location $x = 0$ and time $t = 0$ for periods of 1 year. The solution for stress includes two exponential terms decreasing with depth: one decreasing with $e^{-\gamma z}$ and the other with e^{-kz} as illustrated in top and bottom of Figure 9. The first term is directly proportional to the temperature fluctuation field in the subsurface and clearly dominates near the surface when z is in the order of the temperature skin depth $1/\gamma$. For larger z the second term dominates. The phase for compressional stresses of the first term is the same as for the subsurface temperature field. The phase delay for the second term compared to the surface temperature is constant at $-5\pi/4$. When comparing with Berger's publication, one has to keep in mind that compressional stress $-\sigma$ and extensional strain ε show the same variation with depth. The phase delay for the first near-surface term is also the same for $-\sigma$ and ε. However, the phase delays of the second term are different being $-5\pi/4$ for $-\sigma$ and $-\pi/4$ for ε. When assuming a constant sensitivity with depth, the integrated first term for stress is proportional to $(-1 + i)/2\gamma$ (phase delay $-\pi/4$) while the second term integrates to a value proportional to $(1-i)/\gamma$ being by a factor of $1+\nu$ larger than the first term but with opposite phase.

Table 1. Thermal Diffusivity, Resulting Skin Depth, and Delay Time of a Periodical Surface Temperature Field for Daily and Annual Periods[a]

κ in mm^2/s	Period	γ in m^{-1}	Skin Depth $1/\gamma$ in m	Delay Time $1/\omega$ at Depth $1/\gamma$
0.3	1 annual	0.54	1.9	58d
	1 daily	10.4	0.10	3.8h

[a]Thermal diffusivity is derived from the temperature data in Figure 8.

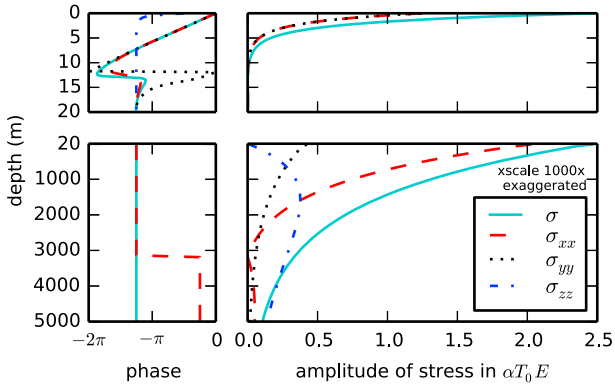

Figure 9. Stress due to temperature changes in the subsurface for a period of 1 year and for $t = 0$, $x = 0$, and $\nu = 0.2$. (top) The y axis scales from 0 to $\approx 10/\gamma$ for $\gamma = 0.54\ \mathrm{m}^{-1}$. (bottom) The scale ranges up to a depth of π/k for $k = 2\pi/10$ km. The scale of the x axis in the bottom right is exaggerated by a factor of 1000 compared to the displayed scale. The phases are displayed for compressional stresses. In the bottom left figure, phases of stresses in y and z directions are the same as for the stress invariant. Figure 9 (top) is dominated by the first term and Figure 9 (bottom) by the second term of equation (11).

4.3. Relationship Between Compressional Stress and Relative Velocity Change

The next step is to discuss the relationship between stress and velocity. Velocity variations induced by stress can be caused by opening and closing of cracks in the material. Therefore, rheology models on microscopic scale were developed by different authors [e.g., *Budiansky and O'Connell*, 1976; *Lyakhovsky et al.*, 1997]. We want to follow here a macroscopic approach based on the expansion of the energy-strain function to cubic terms in strain leading to the third-order elastic constants. By measuring velocity variations due to uniaxial tension or hydrostatic pressure, the third-order elastic (TOE) constants can be determined for different materials [*Hughes and Kelly*, 1953; *Toupin and Bernstein*, 1961; *Thurston and Brugger*, 1964]. TOE constants of rocks are found to be very high compared to the second-order elastic Lamé constants [*Winkler and Liu*, 1996; *Winkler and McGowan*, 2004]. This means seismic velocities in rock are relatively sensitive to stress changes as indicated by the increase of velocity with depth in the subsurface. We estimate the relative velocity change due to compressional stress σ_c with the help of experimentally determined values of $\partial\rho v^2/\partial\sigma_c$:

$$\frac{\Delta v}{v} = \frac{\partial v}{v\partial\sigma_c}\Delta\sigma_c = \frac{\partial\rho v^2}{2\rho v^2\partial\sigma_c}\Delta\sigma_c = b\frac{\partial\rho v^2}{\partial\sigma_c}\frac{(1-\nu)\Delta\sigma_c}{E}. \tag{12}$$

ρv^2 is the shear modulus for S waves and the P wave modulus for P waves. When using the relationships between different elastic moduli $\rho v_s^2 = E/2(1+\nu)$ and $\rho v_p^2 = E(1-\nu)/(1+\nu)(1-2\nu)$ [*Birch*, 1961, Table 4], constant b can be expressed as

$$b = \begin{cases} \frac{(1+\nu)(1-2\nu)}{2(1-\nu)^2} \approx 0.6 & \text{for } P \text{ waves and } \nu = 0.2\,, \\ \frac{(1+\nu)}{(1-\nu)} \approx 1.5 & \text{for } S \text{ waves and } \nu = 0.2\,. \end{cases}$$

Moreover, we assumed $\partial\rho = 0$ in equation (12) because the effect of density change is negligibly small compared to the effects of stressing due to $\partial\rho v^2/\partial\sigma_c \gg 1$ (Table 2). Combining equations (11) and (12) with $\Delta\sigma_c = -\sigma$ we get

$$\frac{\Delta v}{v}(x,z,t) = b\alpha\frac{\partial\rho v^2}{\partial\sigma_c}T(x,z=0,t)\left[2e^{-(1+i)\gamma z} - (1+\nu)(1-i)\frac{k}{\gamma}e^{-kz}\right]. \tag{13}$$

When only considering the first term, which is reasonable for a sensitivity kernel decreasing rapidly with depth, the equation further simplifies to

$$\frac{\Delta v}{v}(x,z,t) = 2b\alpha\frac{\partial\rho v^2}{\partial\sigma_c}T(x,z,t)\,. \tag{14}$$

Table 2. $\partial\rho v^2/\partial\sigma_c$ as an Expression of Third-Order Elastic Constants, Linear Thermal Expansion Coefficient, and the Resulting Relative Velocity Change Due to Temperature Change Predicted by Our Model Using Equation (14) for Different Rock Materials[a]

Material	$\frac{\partial\rho v^2}{\partial\sigma_c}$	α in 10^{-6} K^{-1}	$\frac{\Delta v}{vT}$ in %K^{-1}
Berea sandstone #1	320, 480, 160[b]	10[d]	0.36, 1.44, 0.48
Indiana limestone	240, 160, 80[b]	8[d]	0.22, 0.38, 0.20
Westerly granite	670, 160, 40[c]	8[d]	0.60, 0.38, 0.10

[a]Reproduced are the values for P waves and the two modes of S waves for uniaxial stress. $\partial\rho v^2/\partial\sigma_c$ for hydrostatic stress is even higher up to a factor of 10.
[b]*Winkler and McGowan* [2004].
[c]*Winkler and Liu* [1996].
[d]*Skinner* [1966].

We roughly estimate the temperature effect on seismic velocities due to the $\exp(-\gamma z)$ term in Table 2 with equation (14). These values seem to become very high for temperature fluctuations up to 30 K, but we have to consider that such velocity variations are only observed near the surface. We still need to link the local velocity changes in the subsurface to the observed velocity changes by determining sensitivity kernels of our measurements. Although equation (14) is a reasonable approximation, we will use equation (13) with both terms for calculating the local velocity changes.

4.4. Autocorrelation Sensitivity Kernels

We assume here that the scattered waves recorded by the autocorrelation function are mainly body waves. This assumption is supported by simulations of *Obermann et al.* [2013] accentuating the dominance of body waves against surface waves for late times and high heterogeneity. In the long-time limit the scattered waves can be described in the diffusion regime with the normalized energy distribution $P_{\text{diff}}(\boldsymbol{r}, t)$ in the absence of absorption given by, e.g., *Paasschens* [1997, equation (1)]. $P_{\text{diff}}(\boldsymbol{r}, t)$ is a function of the distance to the source $r = |\boldsymbol{r}|$ and traveltime t. Furthermore, it depends on the diffusion coefficient $D = cl/3$ with velocity c and mean free path l. Because the traveltimes of the waves in our observations are quite small in the order of the mean free time l/c, this approximation is not strictly valid anymore and we have to consider low-order scattered waves, too. For this we use the analytic approximation of the solution for three-dimensional radiative transfer [*Paasschens*, 1997]:

$$P_{\text{rt}}(\boldsymbol{r}, t) = \exp\left(-\frac{ct}{l}\right)\left[\frac{\delta(r-ct)}{4\pi r^2} + \left(\frac{4}{3}\pi lc\right)^{-\frac{3}{2}}\left(1-\frac{r^2}{c^2t^2}\right)^{\frac{1}{8}} t^{-\frac{3}{2}} G\left(\frac{ct}{l}\left(1-\frac{r^2}{c^2t^2}\right)^{\frac{3}{4}}\right) H(ct-r)\right] \quad (15)$$

$$\text{with } G(x) = e^x\sqrt{1+\frac{2.026}{x}}\,.$$

The term with the Dirac delta function δ describes the direct wave, while the other term describes scattered waves. In the limit case $r, l \ll ct$ equation (15) transforms to the corresponding equation for the diffusion approximation. The traveltime kernel for the autocorrelation in the diffusion approximation is a special case of the kernel for the cross-correlation function for colocated source and receiver [*Pacheco and Snieder*, 2005] and given by

$$K_{3\text{-D}}(\boldsymbol{r}, t) = \frac{1}{P_0(t)}\int_0^t P(\boldsymbol{r}, t-t')\,P(\boldsymbol{r}, t')\,\mathrm{d}t'\,. \quad (16)$$

Planès et al. [2014] derived this equation independently based on scattering theory. $P_0(t)$ is a normalization constant. In the diffusion approximation it is given as $P(\boldsymbol{0}, t)$, the energy of the wave field at the position of the receiver at time t. $K_{3\text{-D}}(\boldsymbol{r}, t)$ represents the time of multiple-scattered waves spent inside an infinitesimal volume at location $\boldsymbol{r}$—under the condition that the waves start at the receiver and are detected by the receiver after the traveltime t. According to the definition of $K_{3\text{-D}}$, the traveltime can be expressed as the integral

$$t = \int_V K_{3\text{-D}}(\boldsymbol{r}, t)\,\mathrm{d}\,\boldsymbol{r}^3 \quad (17)$$

over the whole volume V [*Pacheco and Snieder*, 2005]. *Pacheco and Snieder* [2005, equation (19)] show how to calculate the traveltime change as a function of slowness perturbation in the medium with the help of equation (17). The result, rewritten, connects the observed velocity changes ϵ from section 3 with the local velocity changes $\Delta v/v(\boldsymbol{r})$:

$$\epsilon(t) = \frac{1}{t}\int_V K_{3\text{-D}}(\boldsymbol{r}, t)\frac{\Delta v}{v}(\boldsymbol{r})\mathrm{d}\boldsymbol{r}^3\,. \quad (18)$$

Furthermore, *Pacheco and Snieder* [2005] give the solution for the autocorrelation kernel in the diffusion approximation as

$$K_{3\text{-D,diff}}(\boldsymbol{r}, t) = \frac{1}{2\pi Dr}\exp\left(\frac{-r^2}{Dt}\right)\,. \quad (19)$$

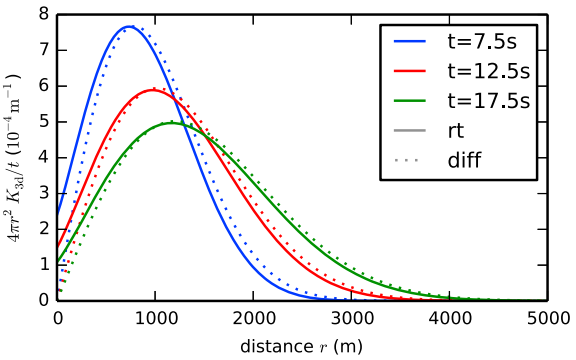

Figure 10. Sensitivity kernel K_{3-D} as a function of distance for traveltimes $t = 7.5$ s, 12.5 s, and 17.5 s with $c = 1$ km/s and $l = 500$ m. The kernels diverge for $r \rightarrow 0$ and are therefore multiplied by $4\pi r^2$ to represent the sensitivity to an infinitesimal spherical shell volume. Furthermore, the kernels are divided by t.

Equation (19) can be derived by inserting equation (1) from *Paasschens* [1997] without absorption into equation (16). For calculating the kernel in the radiative transfer approximation, we use the definition of the kernel in the diffusion approximation in equation (16) as done by *Planès et al.* [2014]. This neglects the sensitivity of direct waves because equation (16) has been derived in the diffusion approximation, but the radiative transfer allows adding sensitivity of low-order scattered waves. A disadvantage of this approach is that $P_0(t) = P(\mathbf{0}, t)$ is not valid anymore under the condition that equation (17) holds true. We circumvent this problem by a renormalization of the kernel. $P_0(t)$ is then given by

$$P_0(t) = \frac{1}{t}\int_V \int_0^t P(\boldsymbol{r}, t-t')\,P(\boldsymbol{r}, t')\,\mathrm{d}t'\mathrm{d}\boldsymbol{r}^3\,. \tag{20}$$

We finally calculate the 3-D autocorrelation kernel in the radiative transfer approximation by inserting equations (15) and (20) into equation (16). The kernel calculated in this way is not exact even in the radiative transfer approximation, because first we use the analytic approximation given by equation (15) and second the sensitivity of the direct wave term is not considered. Still, the kernel is more reliable than the kernel in the diffusion approximation because it includes correction terms for low-order scattering.

The integration is performed partly analytically for terms involving the Dirac delta function and partly numerically (Appendix C). The 3-D solution for the autocorrelation kernels are displayed in Figure 10 for $c = 1$ km/s and $l = 500$ m and three different traveltimes. With the approximation that the temperature T does not vary laterally in the main scope of the sensitivity kernel ($\cos kx \approx 1$ in equation (13)), $\Delta v/v$ becomes a function of just z and t. We can therefore further integrate the kernel in x and y directions to isolate the depth dependence. We choose a cylindrical coordinate system with radius ρ and depth z for this purpose. Equation (18) then reads

$$\epsilon(t) = \frac{1}{t}\int_0^\infty K_z(z,t)\frac{\Delta v}{v}(z)\mathrm{d}z \tag{21}$$

with

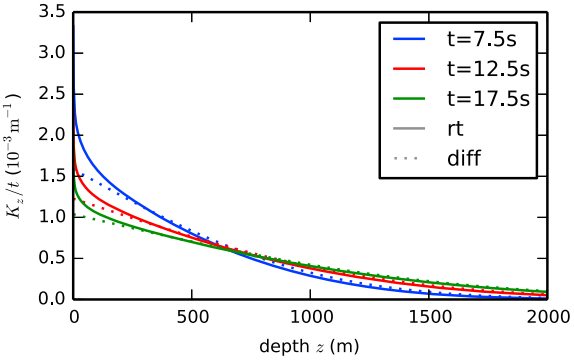

Figure 11. Sensitivity kernel K_z divided by t for traveltimes $t = 7.5$ s, 12.5 s, and 17.5 s with $c = 1$ km/s and $l = 500$ m. Only the regularized version of the kernel is shown. In Appendix C we show that the contribution of the irregular part of the kernel to the modeled velocity change is negligible.

$$\begin{aligned} K_z(z,t) &= 2\int_0^\infty 2\pi\rho K_{3\text{-D}}\left(\sqrt{\rho^2+z^2}, t\right)\mathrm{d}\rho \\ &= 2\int_z^\infty 2\pi r K_{3\text{-D}}(r,t)\mathrm{d}r\,. \end{aligned} \tag{22}$$

Insertion of equation (19) and rewriting the integral with the substitution $r = r'\sqrt{Dt}$ gives us the analytic solution in the diffusion approximation

$$K_{z,\mathrm{diff}}(z,t) = \sqrt{\frac{\pi t}{D}}\left(1 - \mathrm{erf}\left(\frac{z}{\sqrt{Dt}}\right)\right) \tag{23}$$

with the error function $\mathrm{erf}(x) = 2/\sqrt{\pi}\cdot\int_0^x \exp(-x^2)\mathrm{d}x'$. Figure 11 compares this solution with the numerical integration for radiative transfer. As expected waves arriving

Table 3. Model Parameters and Assumed Values

Temperature Field		
Angular frequencies	ω_d, ω_a	$2\pi/1d, 2\pi/1a$
Amplitudes	T_{0d}, T_{0a}	6 K, 19 K
Skin depths	$1/\gamma_d, 1/\gamma_a$	10 cm, 1.9m
Wave number	k	$2\pi/10$ km
Elastic Properties of the Medium		
Poisson's ratio	ν	0.2
Factor (Poisson's ratio)	$b(\nu)$	0.6–1.5
Linear thermal expansion	α	$10^{-6}m^{-1}$–$10^{-5}m^{-1}$
Velocity change due	$\partial\rho v^2/\partial\sigma_c$	200–1000 (uniaxial)
to stress		500–5000 (hydrostatic)
Scattering Parameters for Sensitivity Kernel		
Velocity	c	1 km/s
Mean free path	l	500 m

at earlier times have a higher sensitivity to velocity changes at shallow depth than later arriving waves. Low-order scattered waves in the radiative transfer solution further intensify the sensitivity close to the receiver.

4.5. Periodic Velocity Changes—Observed and Modeled

Finally, we are in the position to calculate observed relative velocity changes predicted by our model. Parameters defining the model are summarized in Table 3. The parameters of the temperature field determine its spatial characteristics, namely, the phase and amplitude. They are determined from temperature data from station CHO2 as described in section 4.1. The wave number k of the temperature field is chosen as $2\pi/10$ km to reflect the influence of the ocean that we assume to remain at constant temperature. With the elastic properties of the medium, we can determine the stress field in the subsurface and infer the relative change of seismic velocities with equation (13). The spatial characteristics of the local velocity change are just controlled by the parameters of the temperature field. Except for k, the parameters of the temperature field are determined well by experiments. Poisson's ratio is set to 0.2 resulting in values of b in equation (12) equal to 0.6 for P waves and 1.5 for S waves. For the scattered mixture of wave types that we analyze in the autocorrelation function, b is between these two values. The velocity change due to stress $\partial\rho v^2/\partial\sigma_c$ is not very well determined even if we would know the material and the polarization properties of the contributing waves. We choose $b = 1.5$, $\alpha = 10^{-5}$ m^{-1}, and $\partial\rho v^2/\partial\sigma_c = 5000$ (hydrostatic pressure changes) from the upper end of the possible intervals maximizing the estimate of the temperature-dependent velocity changes. These three factors have a linear impact on the amplitude of the modeled local velocity changes. They do not influence the phase delay (equation (13)). Note that the chosen value for $\partial\rho v^2/\partial\sigma_c$ is 10 times higher than the largest value presented in Table 2. This corresponds to the exceptional sensitivity observed at PATCX. Moreover, the values in Table 2 are lab estimates for compact rocks. The nonlinearities giving rise to the stress sensitivity are clearly higher in sediments. Together with the autocorrelation depth sensitivity kernels that are determined by the scattering parameters and equation (21), we finally calculate the predicted velocity change. Here we choose $c = 1$ km/s as a near-surface velocity and $l = 500$ m for the scattering mean free path. This is a rough guess based on information from volcanoes [*Wegler and Lühr*, 2001; *Yamamoto and Sato*, 2010] as there is no information available from this area or one with similar conditions.

A comparison of the modeled and observed daily and annual periodic velocity changes is presented in Table 4 for 4 Hz to 6 Hz. The modeled values are calculated for the lag times 7.5 s, 12.5 s, and 17.5 s. These lag times represent the middle of the 5 s long lag time intervals used for the observations of velocity changes of daily periodicity. For annual periodicity six observed values from the overlapping 2 s long time windows

Table 4. Comparison of Modeled and Observed Daily and Annual Periodic Velocity Changes (Amplitude ϵ_P and Phase Delay $t_P - t_{temp}$) for 4–6 Hz and Different Lag Times

		Model		Observation	
Period	Lag Time	Phase d.	Amplitude	Phase d.	Amplitude
1 day	7.5 s	2.8 h	0.058%	1.5 h	0.09%
	12.5 s	2.8 h	0.037%	3.3 h	0.02%
	17.5 s	2.8 h	0.028%	14.5 h	0.02%
1 year	7.5 s	41 d	0.26%	(25 ± 11) d	(0.29 ± 0.06)%
	12.5 s	41 d	0.17%	(38 ± 12) d	(0.17 ± 0.03)%
	17.5 s	41 d	0.13%	(33 ± 4) d	(0.19 ± 0.04)%

from Figure 6 are averaged to determine the mean value and its sample standard deviation for each of the 5 s long time windows. The first-order observation that amplitudes decrease with lag time both for daily and annual periods can be reproduced by the model. The amplitude values roughly agree within a factor of 2. The modeled annual phase delay is 41 days and therefore just between 3 and 16 days away from the mean of the observed phase delays in the three lag time windows. The modeled daily phase delay is 2.8 h and close to the observed value at 12.5 s lag time. The phase delays for the two other lag times are not predicted well.

The biggest impact on the modeled phase delay originates from the sensitivity kernels. The phase delay is mainly determined by the parameters c and l, still it does not change significantly for reasonably chosen values of c and l. Furthermore, the phase delay is still approximately constant over lag times (as in Table 4) for different values of c and l.

Despite the poor fit of some observations, the model shows that the measured daily and annual temperature variations are within the range of values that are to be expected for thermally induced stress changes. We believe that the temperature field is well determined from the data of the nearby station CHO2. There are three sources of uncertainty in our model that could cause discrepancies. First and foremost, the assumption of the horizontal confinement that directly relates expansion to stress might be inappropriate. *Ben-Zion and Leary* [1986] included an unconsolidated surface layer in their model that takes part in the heat conduction but does not transfer stresses and would thus not influence velocities. Our choice not to include such a layer is based on the observation of sediment that is firmly cemented by salt crystals at the surface. The second assumption of our model that is not well constrained is the wavelength of the spatial temperature variation. Changing k affects mostly the ratio between the terms in equation (13). But as the model is dominated by the first term, the results will not change significantly for a large range of k. Finally, the third assumption with considerable uncertainty is that information about velocity changes is carried by body waves that propagate in a medium with depth-independent mean free path. Our choice of body wave kernels was motivated by the observed lapse time dependence of the velocity changes. Surface wave propagation would not be consistent with this observation but could in turn explain the frequency dependence. In fact *Obermann et al.* [2013] showed that the sensitivity of measurements with scattered coda waves is a combination of surface and body wave sensitivity with time-dependent partitioning that gradually transitions from surface to body wave sensitivity with increasing lapse time. Such an effect would indeed allow to explain the small phase delays at early lag times for daily periods as well as for annual periods in some frequency bands. The exceptionally high phase delay of 14.5 h for 17.5 s lag time and daily periods could be explained by a reduced sensitivity for the topmost layer ($\approx$10 cm) and/or a much larger value of the temperature wave number k because of the influence of small-scale topographic effects for daily periods. Then the second term in equation (13) would dominate for daily periods but the first term for annual periods. This would explain why the observed lag time has the same phase delay of $5\pi/4$ (corresponding to 15 h) as the second term of the stress distribution. However, the measurement at 17.5 s lapse time has a significant uncertainty. The relatively strong fluctuations of the frequency and lapse time characteristics of our measurements (Figure 6) partly result from deterministic arrivals in the autocorrelations. This could be responsible for the extraordinary high phase delay of low-frequency autocorrelations at 13 s that appear as outliers in our model that is valid for an ensemble average only.

We summarize that key features and rough amplitudes of our observations can be reproduced by the model. Periodic velocity variations result from thermal stresses in the uppermost 10 m. Even high deviations from average observations for some lag times and frequencies could be explained by sensitivity kernels, resulting from direct reflections, surface wave contributions, or locally varying scattering parameters.

5. Conclusions

By using autocorrelations of seismic noise, we are able to observe velocity variations that correspond to changes in rheological properties caused by temperature variations and ground shaking. As previously reported for other earthquakes [e.g., *Wegler et al.*, 2009], we observe a coseismic decrease of seismic velocities in and around the fault zone of the Tocopilla earthquake. The amplitude of this drop decreases with distance but shows large scatter. Velocity changes and peak ground acceleration (PGA) measured at different seismometer locations are not correlated in any simple way.

At station PATCX we observe a strong coseismic decrease with the Tocopilla event despite the comparatively large distance from the fault area and the small PGA. This indicates a high sensitivity of the subsurface velocity to shaking. The observation of velocity changes coincident with other regional earthquakes confirms the high sensitivity and allows to investigate the relation between PGA and the amplitude of the velocity decrease without the need to involve different stations. We identify a linear correlation between PGA and the observed velocity changes at PATCX. This means that the coseismic changes are due to shaking and consequent damage of the near-surface material and not related to changes of the ambient static stress. Previous attempts to establish a relation of $\Delta v/v$ with PGA or dynamic strain suffered from the necessity to include data from different stations as usually the distribution of changes following a single event are analyzed [e.g., *Sawazaki and Snieder*, 2013]. This shows that the local subsurface conditions have a major effect on the amplitude of the velocity changes. As the velocity changes are due to changes in the elastic moduli that are an important quantity in earthquake engineering, the slope of the PGA-$\Delta v/v$ relation might add important information to the site characterization in seismic hazard analysis. A high sensitivity of the subsurface material at station PATCX is also found for compressional stress. We observe periodic daily and annual velocity changes that we model with stress induced by atmospheric temperature changes. This model takes into account the chain from the subsurface temperature field → subsurface stresses → local velocity variations → observed velocity changes. The central relation between stress and velocity uses third-order elastic constants as a mathematical description of the physical process that introduces nonlinearity in the elastic behavior.

The third observation that is important for understanding the physical origin of the velocity changes is the recovery process of the coseismic changes. Following the Tocopilla earthquake, we observe a recovery process of exponentially increasing velocity with a duration of 2 years at station PATCX. Recovery following the smaller regional events is faster in the order of days to 1 month. These three observations—high sensitivity of velocity to shaking (PGA), pronounced velocity changes due to thermal stress, and postseismic recovery integrate in a model that relates the elastic moduli to compliant porosity and microcracks. The outstanding property of the material at station PATCX is the firm cementation of salt at the surface resulting in an above-average consolidated layer at shallow depth supporting stress. The temperature changes therefore change the seismic velocity through the straining of compliant pores as described by *Shapiro* [2003] and *Shapiro and Kaselow* [2005] and as is reflected in the third-order elastic constants. Shaking causes damage and the opening of compliant pores and microcracks. Healing is the process of gradually closing these cracks again and reestablishing the cementation. The salt content in the sediments at PATCX is therefore likely to be the major reason for the high sensitivity of the velocity changes to stress and shaking.

Appendix A: Similarity Matrices for Stations PB04 and PB05

Figure A1 shows the similarity matrices of stations PB04 and PB05 located near the maxima of the slip distribution of the Tocopilla earthquake. The matrices show the results in the 10–15 s time window of the autocorrelation function which is calculated in the 1–3 Hz frequency band. Clearly visible is the coseismic velocity decrease at the time of the Tocopilla earthquake and the subsequent recovery of the seismic velocity.

Appendix B: Berger's Solution for Thermoelastic Strain

We reproduce here Berger's solution of equation (8) for a periodic surface temperature field with the approximation $k \ll \gamma$ and under consideration of the plane strain assumption. *Berger* [1975, equation (8)] used a different coordinate system, a different definition of γ, and a different surface temperature field $T(x, z = 0, t)$. We rewrite his equations for the principal strains with our definitions:

$$\varepsilon_{xx} = \frac{1+\nu}{1-\nu}\frac{k}{(1+i)\gamma}\left\{(2(1-\nu)-kz)e^{-kz} - \frac{k}{(1+i)\gamma}e^{-(1+i)\gamma z}\right\}\alpha T(x, z=0, t)$$
$$\varepsilon_{zz} = \frac{1+\nu}{1-\nu}\left\{-\frac{k}{(1+i)\gamma}(2\nu-kz)e^{-kz} + e^{-(1+i)\gamma z}\right\}\alpha T(x, z=0, t)\,. \tag{B1}$$

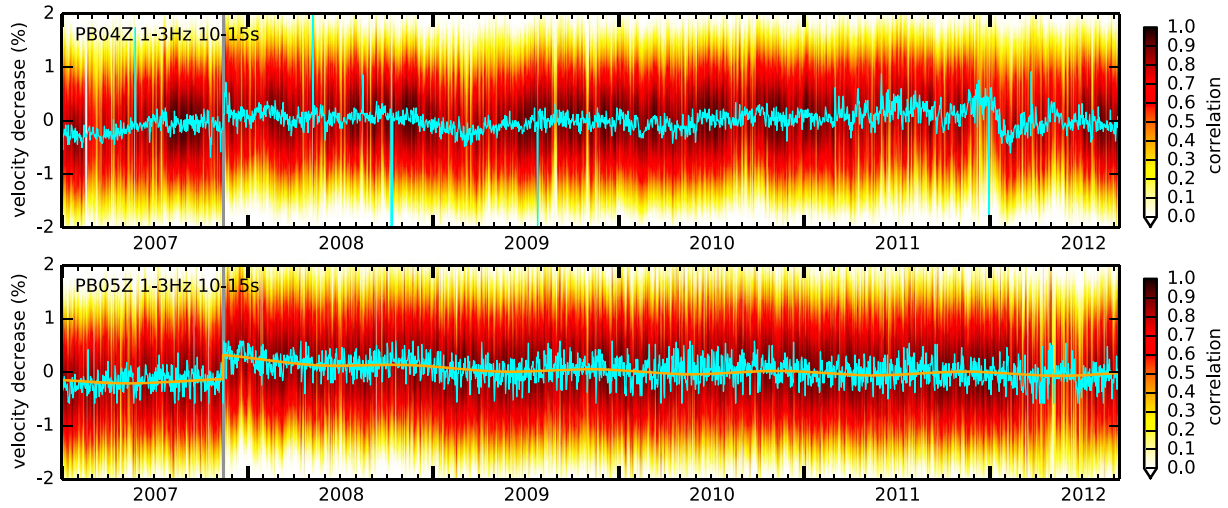

Figure A1. Similarity matrices of the autocorrelation function for stations PB04 and PB05 (frequency band 1−3 Hz, time window 10−15 s). The vertical bar marks the time of the Tocopilla earthquake. Maxima of the similarity matrices for each day are connected by a cyan line. While station PB04 shows only a short-term velocity decrease because of the Tocopilla earthquake, the velocity decrease of station PB05 does not recover until around 2 years after the event. The orange line is a fit of the long-time changes at the similarity matrix. The long-time changes are described by the empirical model of equation (4) plus a constant velocity decrease caused by the Tocopilla earthquake.

Appendix C: Radiative Transfer Kernel for Autocorrelation

We want to insert equation (15) into equations (16) and (22) and perform the integrations to derive the 3-D and depth sensitivity kernels for autocorrelation functions in the radiative transfer approximation. We define three terms *A*, *B*, and *C* in the energy distribution given by

$$P(\boldsymbol{r},t)=\overbrace{\exp\left(-\frac{ct}{l}\right)}^{A(t)}\left[\overbrace{\frac{\delta(r-ct)}{4\pi r^2}}^{B(t,r)}+\overbrace{\left(\frac{4}{3}\pi lc\right)^{-\frac{3}{2}}\left(1-\frac{r^2}{c^2t^2}\right)^{\frac{1}{8}}t^{-\frac{3}{2}}G\left(\frac{ct}{l}\left(1-\frac{r^2}{c^2t^2}\right)^{\frac{3}{4}}\right)H(ct-r)}^{C(t,r)}\right]$$

which leads to

$$K_{3\text{-D,rt}}(\boldsymbol{r},t)=\frac{1}{P_0(t)}\int_0^t P(\boldsymbol{r},t-t')P(\boldsymbol{r},t')\mathrm{d}t'=\frac{A(t)}{P_0(t)}\int_0^t B(t-t')B(t')+\left[B(t-t')C(t')+B(t')C(t-t')\right]+C(t-t')C(t')\mathrm{d}t'. \tag{C1}$$

There are three contributions to the kernel. First, waves scattered just one time at position $\boldsymbol{r}$ (term *BB*), then waves not scattered while traveling to $\boldsymbol{r}$ but scattered while traveling back or vice versa (terms *BC*), and finally waves scattered on the way to $\boldsymbol{r}$ and back (term *CC*). We will name the resulting contributions to the kernel K_1, K_2, and K_3. The last term can be integrated numerically without problems to get K_3 and $K_{z,3}$:

$$K_3(\boldsymbol{r},t)=\frac{A(t)}{P_0(t)}\int_0^t C(t-t',r)C(t',r)\,\mathrm{d}t'\,.$$

The first integration for the second term collapses because of the Dirac delta function:

$$K_2(\boldsymbol{r},t)=\frac{A(t)}{2\pi r^2cP_0(t)}C\left(t-\frac{r}{c},r\right)\,.$$

Inserting into equation (22) gives

$$K_{z,2}(z,t)=\frac{2A(t)}{cP_0(t)}\int_z^\infty\frac{C\left(t-\frac{r}{c},r\right)}{r}\,\mathrm{d}r\,.$$

We can integrate again numerically but have to be careful because for $z \to 0$ the kernel diverges. We exclude therefore a small hemispherical proximity with radius ϵ' when integrating and define

$$K'_{z,2}(z,t) = \frac{2A(t)}{cP_0(t)} \int_{\max(z,\epsilon')}^{\infty} \frac{C\left(t - \frac{r}{c}, r\right)}{r} \mathrm{d}r$$

which can be integrated without problems. The observed velocity change ϵ_2 due to K_2 can then be calculated with equations (18) and (21) as

$$\epsilon_2(t) = \frac{1}{t}\left[\frac{2A(t)}{cP_0(t)}\epsilon' C(t,0)\frac{\Delta v}{v}(\mathbf{0}) + \int_0^{\infty} K'_{z,2}(z,t)\frac{\Delta v}{v}(z)\mathrm{d}z\right].$$

The first term will have a vanishing contribution if ϵ' is chosen small enough. This leaves us with the first term in equation (C1). The term includes two Dirac delta functions, so the first integration still leaves one:

$$K_1(\boldsymbol{r},t) = \frac{A(t)\delta(r - ct/2)}{P_0(t)(4\pi r^2)^2 c}.$$

Under the assumption of validity of equation (16) the calculated 3-D kernel for single scattering is sensitive only to a spherical shell volume at a distance of $ct/2$—the location where it is scattered. This is obviously not correct. The kernel should be sensitive to the whole spherical volume with a radius of $ct/2$. This fact reflects the tradeoff of using the definition of the kernel given by equation (16) which is strictly valid only in the diffusion approximation. Performing the second integration over depth gives a nonzero, constant depth kernel for all $z \le ct/2$

$$K_{z,1}(\boldsymbol{z},t) = \frac{2A(t)H(ct/2 - z)}{\pi P_0(t)c^4 t^3}.$$

For reasonable scattering parameters c and l the contribution of K_1 and $K_{z,1}$ to the whole kernels is insignificant. The contributing terms for the 3-D and depth kernels for radiative transfer and autocorrelation are

$$K_{3\text{-D, rt}} = K_2 + K_3,$$
$$K_{z,\mathrm{rt}} = K'_{z,2} + K_{z,3}.$$

Acknowledgements
T. Richter thanks DFG (Deutsche Forschungsgemeinschaft) for funding. Data processing was performed with the help of the package ObsPy [*Beyreuther et al.*, 2010] and the SciPy tools [*Jones et al.*, 2001] both written for the Python programming language. We thank the IPOC and GEOFON projects for providing the data which can be freely obtained by using the web services at http://geofon.gfz-potsdam.de/. We thank F. Tilmann for proofreading the manuscript. V. Tsai and an anonymous reviewer helped to improve the manuscript with valuable comments.

References

Anderson, O. L., E. Schreiber, R. C. Liebermann, and N. Soga (1968), Some elastic constant data on minerals relevant to geophysics, *Rev. Geophys.*, *6*(4), 491–524, doi:10.1029/RG006i004p00491.

Bach, C. (2010), Sub-millimeter displacement measurements: Creepmeter instrumentation and first results in the central Andean forearc, Diploma thesis, Universität Potsdam, Institut für Geowissenschaften.

Ben-Zion, Y., and P. Leary (1986), Thermoelastic strain in a half-space covered by unconsolidated material, *Bull. Seismol. Soc. Am.*, *76*(5), 1447–1460.

Bensen, G. D., M. H. Ritzwoller, M. P. Barmin, A. L. Levshin, F. Lin, M. P. Moschetti, N. M. Shapiro, and Y. Yang (2007), Processing seismic ambient noise data to obtain reliable broad-band surface wave dispersion measurements, *Geophys. J. Int.*, *169*(3), 1239–1260, doi:10.1111/j.1365-246x.2007.03374.x.

Berger, J. (1975), A note on thermoelastic strains and tilts, *J. Geophys. Res.*, *80*(2), 274–277, doi:10.1029/JB080i002p00274.

Beyreuther, M., R. Barsch, L. Krischer, T. Megies, Y. Behr, and J. Wassermann (2010), ObsPy: A Python toolbox for seismology, *Seismol. Res. Lett.*, *81*(3), 530–533, doi:10.1785/gssrl.81.3.530.

Birch, F. (1961), The velocity of compressional waves in rocks to 10 kilobars: 2, *J. Geophys. Res.*, *66*(7), 2199–2224, doi:10.1029/JZ066i007p02199.

Budiansky, B., and R. J. O'Connell (1976), Elastic moduli of a cracked solid, *Int. J. Solids Struct.*, *12*(2), 81–97, doi:10.1016/0020-7683(76)90044-5.

Hobiger, M., U. Wegler, K. Shiomi, and H. Nakahara (2012), Coseismic and postseismic elastic wave velocity variations caused by the 2008 Iwate-Miyagi Nairiku earthquake, Japan, *J. Geophys. Res.*, *117*, B09313, doi:10.1029/2012JB009402.

Hughes, D. S., and J. L. Kelly (1953), Second-order elastic deformation of solids, *Phys. Rev.*, *92*, 1145–1149, doi:10.1103/physrev.92.1145.

Jones, E., et al. (2001), SciPy: Open source scientific tools for Python. [Available at http://scipy.org/.]

Lyakhovsky, V., Z. Reches, R. Weinberger, and T. E. Scott (1997), Non-linear elastic behaviour of damaged rocks, *Geophys. J. Int.*, *130*(1), 157–166, doi:10.1111/j.1365-246x.1997.tb00995.x.

Maeda, T., K. Obara, and Y. Yukutake (2010), Seismic velocity decrease and recovery related to earthquake swarms in a geothermal area, *Earth Planets Space*, *62*, 685–691, doi:10.5047/eps.2010.08.006.

Meier, U., N. M. Shapiro, and F. Brenguier (2010), Detecting seasonal variations in seismic velocities within Los Angeles basin from correlations of ambient seismic noise, *Geophys. J. Int.*, *181*(2), 985–996, doi:10.1111/j.1365-246x.2010.04550.x.

Nelder, J. A., and R. Mead (1965), A simplex method for function minimization, *Comput. J.*, *7*(4), 308–313, doi:10.1093/comjnl/7.4.308.

Obermann, A., T. Planès, E. Larose, C. Sens-Schönfelder, and M. Campillo (2013), Depth sensitivity of seismic coda waves to velocity perturbations in an elastic heterogeneous medium, *Geophys. J. Int.*, doi:10.1093/gji/ggt043.

Paasschens, J. C. J. (1997), Solution of the time-dependent Boltzmann equation, *Phys. Rev. E*, *56*, 1135–1141, doi:10.1103/physreve.56.1135.
Pacheco, C., and R. Snieder (2005), Time-lapse travel time change of multiply scattered acoustic waves, *J. Acoust. Soc. Am.*, *118*(3), 1300–1310, doi:10.1121/1.2000827.
Planès, T., E. Larose, L. Margerin, V. Rossetto, and C. Sens-Schönfelder (2014), Decorrelation and phase-shift of coda waves induced by local changes: Multiple scattering approach and numerical validation, *Waves Random Complex Media*, *24*(2), 99–125, doi:10.1080/17455030.2014.880821.
Reijs, J., and K. McClay (1998), Salar Grande pull-apart basin, Atacama fault system, northern Chile, *Geol. Soc. London Spec. Publ.*, *135*(1), 127–141, doi:10.1144/gsl.sp.1998.135.01.09.
Rivet, D., M. Campillo, N. M. Shapiro, V. Cruz-Atienza, M. Radiguet, N. Cotte, and V. Kostoglodov (2011), Seismic evidence of nonlinear crustal deformation during a large slow slip event in Mexico, *Geophys. Res. Lett.*, *38*, L08308, doi:10.1029/2011GL047151.
Sawazaki, K., and R. Snieder (2013), Time-lapse changes of P- and S-wave velocities and shear wave splitting in the first year after the 2011 Tohoku earthquake, Japan: Shallow subsurface, *Geophys. J. Int.*, *193*(1), 238–251, doi:10.1093/gji/ggs080.
Schurr, B., G. Asch, M. Rosenau, R. Wang, O. Oncken, S. Barrientos, P. Salazar, and J. P. Vilotte (2012), The 2007 M7.7 Tocopilla northern Chile earthquake sequence: Implications for along-strike and downdip rupture segmentation and megathrust frictional behavior, *J. Geophys. Res.*, *117*, B05305, doi:10.1029/2011JB009030.
Sens-Schönfelder, C., and U. Wegler (2006), Passive image interferometry and seasonal variations of seismic velocities at Merapi Volcano, Indonesia, *Geophys. Res. Lett.*, *33*, L21302, doi:10.1029/2006GL027797.
Sens-Schönfelder, C., and U. Wegler (2011), Passive image interferometry for monitoring crustal changes with ambient seismic noise, *C. R. Geosci.*, *343*(8-9), 639–651, doi:10.1016/j.crte.2011.02.005.
Shapiro, N. M., and M. Campillo (2004), Emergence of broadband Rayleigh waves from correlations of the ambient seismic noise, *Geophys. Res. Lett.*, *31*, L07614, doi:10.1029/2004GL019491.
Shapiro, S. (2003), Elastic piezosensitivity of porous and fractured rocks, *Geophysics*, *68*(2), 482–486, doi:10.1190/1.1567215.
Shapiro, S., and A. Kaselow (2005), Porosity and elastic anisotropy of rocks under tectonic stress and pore-pressure changes, *Geophysics*, *70*(5), N27–N38, doi:10.1190/1.2073884.
Skinner, B. J. (1966), Thermal expansion, in *Handbook of Physical Constants, Geol. Soc. Am. Mem.*, vol. 97, edited by S. P. Clark, pp. 75–96, Geol. Soc. Am., New York.
Snieder, R., A. Grêt, H. Douma, and J. Scales (2002), Coda wave interferometry for estimating nonlinear behavior in seismic velocity, *Science*, *295*(5563), 2253–2255, doi:10.1126/science.1070015.
Takagi, R., and T. Okada (2012), Temporal change in shear velocity and polarization anisotropy related to the 2011 M9.0 Tohoku-Oki earthquake examined using KiK-net vertical array data, *Geophys. Res. Lett.*, *39*, L09310, doi:10.1029/2012GL051342.
Thurston, R. N., and K. Brugger (1964), Third-order elastic constants and the velocity of small amplitude elastic waves in homogeneously stressed media, *Phys. Rev.*, *133*, A1604–A1610, doi:10.1103/physrev.133.a1604.
Toupin, R. A., and B. Bernstein (1961), Sound waves in deformed perfectly elastic materials. Acoustoelastic effect, *J. Acoust. Soc. Am.*, *33*(2), 216–225, doi:10.1121/1.1908623.
Tsai, V. C. (2011), A model for seasonal changes in GPS positions and seismic wave speeds due to thermoelastic and hydrologic variations, *J. Geophys. Res.*, *116*, B04404, doi:10.1029/2010JB008156.
Wegler, U., and B.-G. Lühr (2001), Scattering behaviour at Merapi volcano (Java) revealed from an active seismic experiment, *Geophys. J. Int.*, *145*(3), 579–592, doi:10.1046/j.1365-246x.2001.01390.x.
Wegler, U., and C. Sens-Schönfelder (2007), Fault zone monitoring with passive image interferometry, *Geophys. J. Int.*, *168*(3), 1029–1033, doi:10.1111/j.1365-246x.2006.03284.x.
Wegler, U., H. Nakahara, C. Sens-Schönfelder, M. Korn, and K. Shiomi (2009), Sudden drop of seismic velocity after the 2004 Mw 6.6 mid-Niigata earthquake, Japan, observed with passive image interferometry, *J. Geophys. Res.*, *114*, B06305, doi:10.1029/2008JB005869.
Winkler, K. W., and X. Liu (1996), Measurements of third-order elastic constants in rocks, *J. Acoust. Soc. Am.*, *100*(3), 1392–1398, doi:10.1121/1.415986.
Winkler, K. W., and L. McGowan (2004), Nonlinear acoustoelastic constants of dry and saturated rocks, *J. Geophys. Res.*, *109*, B10204, doi:10.1029/2004JB003262.
Wright, M. H. (1996), Direct search methods: Once scorned, now respectable, in *Numerical Analysis 1995: Proceedings of the 1995 Dundee Biennial Conference in Numerical Analysis*, edited by D. F. Griffiths and G. A. Watson, pp. 191–208, Addison Wesley Longman, Harlow, U. K.
Yamamoto, M., and H. Sato (2010), Multiple scattering and mode conversion revealed by an active seismic experiment at Asama volcano, Japan, *J. Geophys. Res.*, *115*, B07304, doi:10.1029/2009JB007109.
Zhan, Z., V. C. Tsai, and R. W. Clayton (2013), Spurious velocity changes caused by temporal variations in ambient noise frequency content, *Geophys. J. Int.*, *194*(3), 1574–1581, doi:10.1093/gji/ggt170.

Erratum

In the originally published version of this article, on page 17, equation (C1) was printed incorrectly. This error has since been corrected and this version may be considered the authoritative version of record.